

**Conservative Transport Schemes for Spherical Geodesic Grids:
High-Order Reconstructions for Forward-In-Time Schemes**

WILLIAM C. SKAMAROCK

*National Center for Atmospheric Research **

AND MAXIMO MENCHACA

University of Illinois, Champaign-Urbana, Illinois.

16 February 2010

submitted to Monthly Weather Review

Revised 12 May 2010

*The National Center for Atmospheric Research is sponsored by the National Science Foundation.

Corresponding author address: William C. Skamarock, National Center for Atmospheric Research, P.O. Box 3000, Boulder, CO 80307-3000. E-mail: skamaroc@ucar.edu

ABSTRACT

The finite-volume transport scheme of Miura (2007), for icosahedral-hexagonal meshes on the sphere, is extended by using higher-order reconstructions of the transported scalar within the formulation. The use of second and fourth order reconstructions, in contrast to the first-order reconstruction used in the original scheme, results in significantly more accurate solutions at a given mesh density, and better phase and amplitude error characteristics in standard transport tests. The schemes using the higher-order reconstructions also exhibit much less dependence of the solution error on the timestep compared to the original formulation.

The original scheme of Miura (2007) was only tested using a non-deformational time-independent flow. The deformational time-dependent flow test used to examine 2D planar transport in Blossey and Durran (2008) is adapted to the sphere, and the schemes are subjected to this test. The results largely confirm those generated using the simpler tests. The results also indicate that the scheme using the second-order reconstruction is most efficient and its use is recommended over the scheme using the first-order reconstruction. The second-order reconstruction uses the same computational stencil as the first-order reconstruction and thus do not create any additional parallelization issues.

1. Introduction

Equations describing the transport of fluid constituents on the sphere arise in many applications. The spherical geometry introduces a number of complications into the discrete solution of transport equations or, more generally, into fluid-flow solvers. These discretizations require some grid or mesh decomposition of the spherical surface, and a number of options have been explored (Williamson 2007). In this paper we present an extension of the finite volume transport scheme of Miura (2007, hereafter referred to as M07) for use on icosahedral (hexagonal) meshes, and we subject the original and extended schemes to a broader range of tests. Grids based on hexagons allow a more uniform discretization of the sphere compared to the latitude-longitude grids, but the spherical icosahedral grids are nonuniform. Finite volume methods can be directly applied on non-uniform grids, but extensions of these approaches to greater than second order accuracy is difficult, and it is these higher-order accurate extensions that we pursue here.

Within the finite-volume approach, we begin with the flux (conservative) form of the transport equation:

$$\frac{\partial(\rho\psi)}{\partial t} = -\nabla \cdot \mathbf{V}\rho\psi,$$

where ρ is the fluid density, ψ is the mixing ratio of some constituent in the fluid and \mathbf{V} is the fluid velocity. Integration in space, over the control volume (i.e. the finite volume), and in time over the timestep, along with the use of Stokes theorem yields

$$A_i \left(\widehat{\rho\psi}^{t+\Delta t} - \widehat{\rho\psi}^t \right)_i = - \int_t^{t+\Delta t} \int_{\Gamma_i} (\mathbf{V} \cdot \mathbf{n}_i) \rho\psi \, d\Gamma \, dt, \quad (1)$$

where $\widehat{}$ indicates a volume-averaged quantity, Γ is cell boundary, \mathbf{n}_i is the unit vector normal to the cell boundary, and A_i is the cell area. Applied to a discrete mesh, (1) can be written

as

$$\widehat{(\rho\psi)}_i^{t+\Delta t} = \widehat{(\rho\psi)}_i^t - \frac{1}{A_i} \sum_{n_{e_i}} d_{e_i} (\mathbf{V} \cdot \mathbf{n}_{e_i}) \rho\psi \Delta t, \quad (2)$$

where n_{e_i} refers to the edges of the control volume i (in our case the edges of the icosahedral mesh cell i), and d_{e_i} is the length of edge e for cell i . No approximations have been made developing (2) because we have not yet specified how we evaluate the term in the summation.

The second term on the right hand side of (2) is the sum of the fluxes through the control volume edge. M07 approximates the scalar mass flux $d_{e_i} (\mathbf{V} \cdot \mathbf{n}_{e_i}) \rho\psi \Delta t$ as schematically described in the left-hand panel of figure 1. The mass flux is approximated by the mass contained within the shaded area A_m . The area A_m is the area swept out by the edge moving at a constant velocity $-\mathbf{V}$ over a time period Δt . Evaluation of the mass integral over the area is accomplished by first fitting a first-order polynomial to represent the mass distribution in each cell, using the cell-averaged values of a given cell and its neighbors, as depicted in figure 2. The integral of the first order polynomial over A_m equals the shaded area times the polynomial evaluated at the center of mass of A_m . M07 uses the polynomial even when the shaded area extends to regions outside the upstream cell.

The overall accuracy of this scheme is limited by the reconstruction of the scalar mass in a given cell and by the computation of A_m , and M07 approximations are nominally second order accurate. In order to increase the formal order of accuracy, both the reconstruction and the computation of A_m would have to be improved. In applications, however, error from one component of the scheme may dominate that from another, hence possible improvements can follow one of two paths. One can relax the assumption of a constant velocity \mathbf{V} on a given cell edge. Lipscomb and Ringler (2005, hereafter referred to as LR05) and Yeh (2007) both

assume a linear velocity distribution along a cell edge, but use a linear polynomial fit to the mass as in M07. Contrary to M07, both integrate these polynomials only within the cells for which they are constructed. This approach is schematically depicted on the right-hand panel in figure 1. As might be expected, the LR05 integration is significantly more complex and costly. Comparison of the results from the two approaches (M07, and LR05 and Yeh 2007) in simple tests indicate that they produce results of similar accuracy. Indeed, M07 presented his scheme as a less-expensive simplification of LR05 and Yeh (2007). Alternatively, one can increase the order of the polynomial used to represent the scalar mass distribution in a given cell to improve the approximation. In his PhD dissertation, Lashley (2002, hereafter referred to as L02) pursued this approach using second and fourth order reconstructions of the scalar mass field and using the same scalar mass flux area determination as M07. In Lashley’s work, that predated M07, LR05 and Yeh (2007), first-order reconstructions were not considered, but his test results showed that the scheme using the fourth-order reconstruction produced significantly more accurate results compared to the scheme using the second-order reconstruction, and that the fourth-order-based scheme appeared to be more efficient.

In this paper we present results from a scheme using second and fourth-order reconstructions of the scalar mass field that are very similar to those used in L02, and we compare these results to those generated using the first-order reconstruction of M07. We verify the main results of M07 and L02, and present results from more-demanding tests to further discriminate between the schemes to verify their robustness, and to confirm that the computation of A_m is not a major source of scheme error.

2. Transport Scheme

Numerical approach

To integrate the discrete version of (2) we must determine the transport velocity \mathbf{V} , the fluid density ρ and the scalar mixing ratio ψ . In models solving the hydrostatic primitive equations or the Navier Stokes equations, the time-dependent velocity and density fields, along with the discrete mass conservation equation satisfied by these fields, would be computed within the dynamics solver. We will assume that the mass fluxes through the cell edges are given along with the velocities, thus our finite-volume solution to (2), following L02 and M07, reduces to determining the area-averaged value of the mixing ratio ψ in the parallelogram with area A_m (the shaded area) given in the left-hand panel of figure 1. The time integrated mass flux in the summation in (2) is given by $d_{e_i}(\rho \mathbf{V} \cdot \mathbf{n}_{e_i}) \bar{\psi} \Delta t$, where $\bar{\psi}$ is the area-averaged mixing ratio. Our procedure does not directly integrate the scalar mass $d_{e_i}(\mathbf{V} \cdot \mathbf{n}_{e_i}) \overline{\rho \psi} \Delta t$ over this area. We choose to evaluate the area-average mixing ratio $\bar{\psi}$ so that we can maintain consistency between the scalar mass conservation equation and the mass conservation equation. If the mass conservation equation is written in the form (2) (with $\psi \equiv 1$) and integrated with the same time step, the scalar mass could be directly integrated but a higher-order quadrature scheme would be needed for the quadratic quantity $(\rho\psi)$ (see LR05).

In L02, M07, LR05, Yeh (2007) and herein, the area-averaged value is computed by integrating polynomials representing the spatial distribution of ψ over the mass flux area

(A_m in figure 1). For a first-order polynomial

$$\psi = c_0 + c_x x + c_y y, \tag{3}$$

M07 uses a least-squares method to determine the coefficients of the polynomial following Stuhne and Peltier (1996). A least-squares fit to a quadratic polynomial is used to obtain the coefficients for the linear polynomial (3) by M07 and for the results presented herein. Other approaches are possible, including using Stokes method (Tomita et al. 2001) or by fitting planes to the cell-averaged values lying at the vertices of the dual grid (triangles) whose centers are the vertices of the hexagons, and producing cell-averaged values of c_x and c_y by averaging these vertex values (LR05 and Yeh 2007). These approaches produce identical results for perfect hexagons on a plane but may produce different results on the imperfect hexagonal grid on the sphere. We have found very little difference in the absolute errors or error convergence rates in our tests using the different approaches, and we have chosen to use a least-squares fit to determine the coefficients because it is easily extended to higher-order polynomials.

For finite-volume transport schemes that compute mass fluxes by integrating over cell-based reconstructions of the scalar mass, it is important that the integral of the scalar mass over the cell equal the mass in the cell, in this case the (predicted) cell-averaged mass times the cell area, e.g. PPM (Woodward and Colella 1984), flux-form Crowley schemes (Tremback et al. 1987). For the first-order reconstruction schemes using (3), if the cell center is the cell center of mass, and if c_0 is set equal to the cell-averaged value, this constraint is automatically satisfied. For higher-order polynomials this constraint will not be satisfied unless it is part of the polynomial construction because integrals of the higher-order terms over the cell area

will not equal zero. In our approach we compute the polynomial coefficients using a least-squares fit after which we adjust the constant term c_0 such that the constraint is satisfied. L02 also constructs the polynomial using the least-squares fit but he satisfies the constraint by including it directly, as a constraint, in the least-squares procedure. We conclude that both approaches to satisfying the constraint are valid because our results are very similar to those of Lashley.

In L02's weighted-least-squares procedure for fitting the polynomial, he weights the fit to the center point (point 0 in figures 1 and 2) by a factor of 1000 relative to the surrounding points. We have experimented with this weighting for the second, third and fourth-order polynomial fits and verified that the weighting is necessary; if all points are weighted equally the solution accuracy is dramatically degraded. We have also verified that no obvious weighting of the nearest neighbors for the third and fourth-order polynomials (i.e. points 1-7 in figure 2) produces better solutions compared to only weighting the center point, again verifying the results of L02. Guided by these results, we have chosen to require that c_0 be the cell-averaged values for the least-squares-fit polynomial solution, and we accomplish this by writing the polynomial in terms of the difference from the cell-centered value (Majewski et al. 2002). For example, in the case of the second-order polynomial

$$\psi = c_0 + c_x x + c_y y + c_{xx} x^2 + c_{xy} xy + c_{yy} y^2. \quad (4)$$

we set $c_0 = \psi_0$ and construct the least-squares problem using the polynomial

$$\psi - \psi_0 = c_x x + c_y y + c_{xx} x^2 + c_{xy} xy + c_{yy} y^2. \quad (5)$$

In (5) there are 5 unknowns and 6 neighbor points to fit (or 5 in the case of a pentagon), hence the least-squares problem is well-posed for cells possessing ≥ 5 edges. In practice we

observe no discernible difference using (5) or a weighted-least-squares approach using (4) and a weight of 1000 for the center point as in L02. We will also examine results using the fourth-order polynomial

$$\begin{aligned}
\psi - \psi_0 = & c_x x + c_y y + c_{xx} x^2 + c_{xy} xy + c_{yy} y^2 \\
& + c_{xxx} x^3 + c_{xxy} x^2 y + c_{xyy} xy^2 + c_{yyy} y^3 \\
& + c_{xxxx} x^4 + c_{xxxy} x^3 y + c_{xxyy} x^2 y^2 + c_{xyyy} xy^3 + c_{yyyy} y^4
\end{aligned} \tag{6}$$

that has 14 unknowns. For a mesh constructed of hexagons there are 18 points to fit and for a pentagon surrounded by hexagons there are 15 points to fit, so the least-squares problem is well-posed for the hexagonal-icosahedral grid.

We note here that we are treating the cell-averaged scalar values as point values in our polynomial fit, and the need to adjust the polynomial to produce the correct integrated mass for the center cell partly reflects this inconsistency. We could choose to constrain the cell-integrated polynomial to reproduce the cell-average value for each cell used in the polynomial reconstruction (Dr. Hilary Weller, personal communication). We would likely need to strongly weight the central-cell constraint in the least-squares fit given its importance as indicated by L02 and in our investigations. Given the error associated with other aspects of this scheme, such as the area determination and in the projection from sphere to tangent plane (see the next subsection), we would not expect to observe increased accuracy using this approach in general applications.

The integration of the polynomial over the parallelogram (the shaded area in the left-hand panel of figure 1) requires numerical quadrature. For the first-order polynomial this requires evaluating the polynomial value at the center of mass of the parallelogram. We use

a 2D tensor product of 1D Gauss quadrature points and weights for integrating the higher-order polynomials. This requires evaluating the polynomial at n^2 points for a polynomial of order n . The 1D weights and quadrature points are given in table 1 (also see Stroud (1971)).

Integration Sequence

To integrate (2) on the sphere, we begin by defining a 2D tangent plane that intersects the sphere at the center of the cell for which we are producing a reconstruction. The neighboring points used in the reconstruction are projected onto the tangent plane using (preserving) the great-circle distances between the cell-center point and the neighbor points, and using (preserving) the angles at the cell-center point defined by the great-circle arcs between these points and the cell-center point. L02 experimented with a number of approaches for projecting the grid onto a tangent plane and found that the results were relatively insensitive to the options he investigated.

For each cell reconstruction, our least-squares-fit polynomial is defined by

$$P\vec{f} = \tilde{\vec{s}}$$

where

$\vec{s} = [\psi_0, \dots, \psi_m]^T$: Cell-averaged scalar mixing ratios, dimension m .

$\tilde{\vec{s}} = [\tilde{\psi}_0, \dots, \tilde{\psi}_m]^T$: Least-squares-fit cell-averaged scalar mixing ratios, dimension m .

$\vec{f} = [f_0, \dots, f_n]^T$: Coefficients for the polynomial fit ($f_0 = c_0, f_1 = c_x, \dots$), dimension n .

P : Polynomial matrix, P is $(m \times n)$.

To determine the polynomial coefficients \vec{f} as a function of the scalar mixing ratios \vec{s} , we

use a least-squares fit following Strang (1980)

$$\tilde{\vec{f}} = (P^T P)^{-1} P^T \vec{s} = \tilde{B} \vec{s}, \quad (7)$$

where \tilde{B} is an $(n \times m)$ matrix. Note that in practice we solve (7) using a polynomial matrix P constructed from the constrained polynomial where $c_0 = \psi_0$, e.g. (5) and (6), after which we expand the resulting matrix \tilde{B} to include the constant. Following this least-squares solution, we adjust the constant such that the integral of the polynomial over the cell is equal to the cell-averaged value ψ_0 . We denote this new matrix equation as

$$\vec{f} = B \vec{s},$$

where B is the polynomial generator matrix. The computations to define the polynomial for each cell do not depend on the cell values or the velocities, hence prior to the integration we compute the matrix B for each cell and store it for later use.

Next, for each timestep we compute the mass fluxes and update the cell average value using (2). First, we define the following quantities:

\vec{q} : Quadrature points vector of dimension n for the interpolation polynomial.

For example, for the second-order polynomial

$$\vec{q} = [w_j, w_j x_j, w_j y_j, w_j x_j^2, w_j y_j^2, w_j x_j y_j]^T,$$

where w_j are the Gauss quadrature weights (see table 1),

(x_j, y_j) are the Gauss quadrature points, and j implies summation.

$$\vec{g}^T = \vec{q}^T B : \text{Quadrature vector, dimension } m.$$

Given the velocity at a cell edge, the quadrature points (x_j, y_j) can be computed followed by the computation of \vec{q} using the Gauss quadrature weights. Next, the vector \vec{g} is constructed

using \vec{q} and the time-invariant matrix B . The integral of ψ over the area A_m in figure 1 is then evaluated by Gauss quadrature, and cast in terms of an area-averaged value:

$$\begin{aligned}
A_m^{-1} \int_{A_m} \psi dA &= \vec{q}^T \overline{\vec{f}} \\
&= \vec{q}^T B \vec{s} \\
&= \vec{g}^T \vec{s}.
\end{aligned} \tag{8}$$

Following M07, the mass flux for each scalar variable k is evaluated using the vector multiplication $\Delta t \rho u_{\perp} d_{e_i} \vec{g}_{e_i}^T \vec{s}_k$ for each scalar s_k for that cell edge, where $\Delta t d_{e_i} u_{\perp}$ is the area (A_m in figure 1). The start-up cost per timestep is that incurred computing \vec{g} ; thereafter each flux calculation requires only a single vector multiply. This abstraction is meant to be general; \vec{s} can include values from any of the cells in the mesh and \vec{f} can include any order polynomial, so long as the number of unknown coefficients in the polynomial are less than or equal to the number of scalar values (i.e., $m \geq n$).

After all the fluxes used in a scalar update have been computed, we use the monotonic limiter described in Zalesak (1979, (also see Skamarock (2006))) to limit the fluxes and guarantee monotonicity. All of the results presented in this paper use this limiter.

3. Results

Cosine bell

The advection of a cosine bell is described in Williamson et al. (1992), where the advecting wind, representing solid-body rotation, transports the bell once around the sphere returning

it to its initial location. Following Williamson et al. (1992), we define the bell as

$$\psi = \begin{cases} (\psi_0/2) (1 + \cos(\pi r/R)) & \text{if } r < R, \\ 0 & \text{if } r \geq R. \end{cases} \quad (9)$$

where $\psi_0 = 1000$, the bell radius $R = a/3$ and a is the radius of the sphere. The zonal velocity $u = \cos(\lambda) 2\pi a/(12 \text{ days})$ where λ is the latitude. The L_2 and L_∞ error norms are computed in the standard way:

$$L_2 = \left(\sum_{cells} A_{cell} (\psi_{cell} - \psi_{exact})^2 \right)^{\frac{1}{2}} / \left(\sum_{cells} A_{cell} \psi_{exact}^2 \right)^{\frac{1}{2}}$$

$$L_\infty = \max_{cells} |\psi_{cell} - \psi_{exact}| / \max_{cells} |\psi_{exact}|$$

Figure 3 shows the L_2 and L_∞ norms for the cosine bell test case using the first, second and fourth order reconstructions with timestep and grid densities given in table 2. The timesteps and grid densities are the same as those used in M07, and the timesteps are very near the maximum allowable step on a given grid. The first-order reconstruction produces results very close to those presented in M07 figure 4a . They are not identical because we use a different limiter and our grid is a spherical centroidal Voronoi tessalation (see LR05) that also differs from M07. The scheme using the second order reconstruction produces a slightly more accurate solution but almost the same convergence rate compared to first-order reconstruction-based scheme. The scheme using the fourth-order reconstruction produces solutions that are significantly more accurate at a given grid density than those produced using first or second order reconstructions, although it shows a similar overall convergence rate in both norms compared to the schemes using first and second order reconstructions. Figure 4 presents the solutions and solution errors for the schemes using first and second-order reconstructions on a grid with 10242 cells. The maximum errors for the second order

reconstruction are only slightly lower than those using the first-order reconstruction, but the errors are more symmetrically distributed for the second-order reconstruction.

M07 commented on the effect of simulation timestep on the solution error, noting that the error increased significantly with decreasing timestep. Figure 5 depicts the error norms for schemes using the first and second order reconstructions on the 40962-cell mesh with a constant timestep $\Delta t = 50s$. The results from the scheme using the first-order reconstruction reproduce the results in M07 figure 6. The results for the scheme using the second-order reconstruction are very similar to those produced using the variable timestep given in figure 3. The L_2 and L_∞ error norms for these schemes using the 40962-cell mesh are plotted as a function of timestep in figure 6. The scheme using the first-order reconstruction shows a significantly increasing solution error with decreasing timestep, whereas the scheme using the second order reconstruction shows only a very small increase in error for decreasing timestep. M07 attributes the first-order-reconstruction results to the fact that, for these second-order schemes, the high-wavenumber phase speed error increases substantially with decreasing Courant number. We agree with M07 explanation and note that this is a common characteristic of second-order forward-in-time finite-volume schemes (e.g. van Leer (1977); the second order flux-form schemes in Tremback et al. (1987)).

Slotted cylinder

The slotted-cylinder test is the same as the cosine-bell test except the cylinder replaces the cosine bell, and results for this test were presented in LR05. Figure 7 depicts the initial cylinder that has a radius $R = a/2$, slot width $a/6$ and slot length $5a/6$. The simulation

results for the schemes using first and second-order reconstructions are also depicted in figure 7. Because of the discontinuous nature of the cylinder edges, the quality of the results are largely determined by the monotonic limiter, and higher mesh densities result in a sharper depiction of the discontinuity at the cylinder edges. For the schemes using the first and second order reconstructions, the final states are symmetric about the slot when using large timesteps (1800 s on the 40962-cell mesh), and the 40962-cell mesh results are very similar. For the scheme using second-order reconstruction, a reduction in the timestep to 50 s for the 40962-cell mesh results in more smearing of the discontinuity, consistent with more applications of the limiter, but the solution maintains its symmetry about the cylinder slot. For the scheme using the first-order reconstruction and a 50 s timestep on the 40962-cell mesh, significant solution asymmetry about the cylinder slot appears and more smearing of the edge is apparent compared to the scheme using the second-order reconstruction. The results for the first order scheme using the small timestep are very similar to those presented in LR05, particularly the solution asymmetry evident in LR05 figure 9d, and indicate that the low order reconstruction is responsible for these asymmetry errors and not other aspects of the schemes.

Blossey and Durran deformational flow test

In order to provide a more demanding and more realistic test case for these advection schemes, we have adapted the 2D deformational flow test case presented in Blossey and Durran (2008) to the sphere. The test is depicted in figure 8. A background solid-body-rotation flow advects the cosine bell in a counterclockwise direction about the pole, and the

cosine bell is deformed by an additional time-dependent deformational flow. The deformational component is designed such that the circularly-symmetric cosine bell is recovered at the end of each revolution, and the sign of the deformation alternates each revolution. The deformation flow component is given by

$$u_\theta = -\frac{4\pi a}{T} \cos\left(\frac{2\pi t}{T}\right) \frac{1 - (4\phi/\pi)^6}{1 + (4\phi/\pi)^6} \quad (10)$$

where u_θ is the longitudinal velocity, $\phi = \pi/2 - \lambda$ is the co-latitude (λ is the latitude), a is the radius of the sphere and $T = 24$ days is the timescale for the deformational component. The solid-body-rotation velocity is the same as in the cosine-bell test case ($u = \cos(\lambda) 4\pi a/T$), and the velocity scale for the deformational component is the same as that used for the solid-body rotation. The streamfunction used to compute the velocity on the icosahedral grid is adapted from Blossey and Durran (2008):

$$\Psi(\tilde{r}, t) = \frac{4\pi a^2}{T} \left\{ \sin \lambda \pm \cos\left(\frac{2\pi}{T}\right) \left[\frac{\tilde{r}^2}{2} + \frac{1}{96} \log(1 - 16\tilde{r}^2 + 256\tilde{r}^4) - \frac{1}{48} \log(1 + 16\tilde{r}^2) - \frac{\sqrt{3}}{48} \arctan\left(\frac{1 - 32\tilde{r}^2}{\sqrt{3}}\right) \right] \right\}. \quad (11)$$

where $\tilde{r} = \phi/\pi$, and the positive sign is used in the northern hemisphere and the negative sign in the southern hemisphere. On the icosahedral grid, the streamfunction is defined at the vertices of the cell, and the velocity on a cell edge is computed by taking the difference between the streamfunction values at the vertices of the edge divided by the great-circle distance between these vertices. The streamfunction is discontinuous and multi-valued at the equator, so discrete differentiation for edges crossing the equator is accomplished by adding the differences on both sides of the equator taking into account the sign change in (11).

Figure 9 shows the L_2 and L_∞ norms for solutions computed using the timestep and mesh parameters given in table 2 and using first, second and fourth order reconstructions. The norms are plotted for the solutions at time $T/2$ (one revolution) and give the same relative results for scheme comparison as those plotted at time T . The different schemes show approximately second order convergence rates in both the L_2 and L_∞ error norms, with the fourth-order-based scheme showing an overall slightly greater than second order convergence rate, the second-order-based scheme almost exactly second order convergence, and the first-order-based scheme slightly less than second-order convergence. The schemes using second and fourth reconstructions exhibit much lower solution errors compared to the scheme using the first-order reconstruction for a given mesh density, with the fourth-order based scheme possessing solution errors less than that for the first-order based scheme at double the resolution, and errors only slightly higher than the second-order-based scheme at double the resolution.

Plots of the solutions after 2 revolutions are shown in Figure 10. The centerline of the deformation flow is not coincident with the center of the bell, and this is the primary reason for the obvious latitudinal asymmetry in the final shape of the bell for 40962-cell mesh. The asymmetries are very similar to those found in the 2D planar test results reported in Blossey and Durran (2008) in their figures 7-9. The 40962-cell and 163842-cell meshes have average cell-center spacings, relative to the width of the bell, of approximately $R/17$ and $R/32$, and Blossey and Durran (2008) plot their results for grid-spacings of $R/10$, $R/20$, and $R/40$. The solutions for the reconstruction-based schemes presented have accuracy similar to those presented in Blossey and Durran (2008) for a given resolution. The superiority of the schemes using second and fourth order reconstructions over the first-order-reconstruction

based scheme is evident.

Efficiency

In order to assess the overall efficiency of transport schemes, we need to consider the computational cost of the schemes in addition to their accuracy as a function of grid density. There are a number of problems encountered in trying to quantify the cost of schemes, including trying to quantify the effects of possible different codings of the schemes, different compilers and different processor and memory architectures. We cannot address all these problems here, but we have run these tests on a single-processor computer and recorded CPU timing statistics for the main integration in order to give rough estimates of the scheme costs. We have found that for a given grid density, timestep, using our limiter, and transporting a single scalar, the scheme using the second order reconstruction take approximately 1.2 times the CPU time as the scheme using the first-order reconstruction, and the scheme using the fourth-order reconstruction uses approximately 8 times the CPU time of the first-order reconstruction scheme. These approximate scalings hold for the mesh densities used in our tests. As expected, the higher-order reconstructions cost more. The fourth-order reconstructions cost significantly more than the first and second-order reconstructions because of the need to evaluate function values at 16 quadrature points which requires the evaluation of a fourth-order polynomial at each of these points.

We have plotted the L_2 error norms as a function of relative cost using this scaling for the deformational test case in figure 11. The plot indicates that the scheme using the second-order reconstruction will always be more efficient (cost for a given accuracy or accuracy

for a given cost) than the scheme using the first-order reconstruction. The fourth-order reconstruction based scheme is slightly less efficient than the first-order based scheme for L_2 errors higher than approximately 0.05 but it is more efficient for lower errors. Given their better error characteristics, such as solution symmetry (e.g. figures 4, 7 and 10), we recommend using the second order reconstruction in this advection algorithm. The fourth order reconstruction is less efficient than the second-order reconstruction in all cases, and the larger stencil needed by the fourth order reconstruction (figure 2) may have an impact on distributed memory implementations and efficiency compared to the second order reconstruction. Recall that the second-order reconstruction uses the same stencil as the first order reconstruction, thus it should use the same distributed memory implementation as the first-order scheme.

The efficiency of the fourth-order reconstruction, and its attractiveness, might be improved by increasing the efficiency of the polynomial generation or the quadrature. It also should improve relative to the lower-order reconstructions as the number of scalars being advected increases. L02 found that the scheme based on the fourth-order reconstruction was more efficient than that using the second-order reconstruction. Our results differ (see figure 11), but we are using different test cases, and L02 does not provide sufficient information to reproduce his test results.

4. Summary

We have examined M07's 2D transport scheme for spherical icosahedral (hexagonal) meshes, and our extensions to the scheme. We have qualitatively reproduced M07's re-

sults, although with a different flux limiter. Following the thesis of L02, we have produced simulations using higher-order polynomial reconstructions than used in M07, and these reconstructions produce significantly more accurate solutions on a given mesh. The schemes using the higher order reconstructions also produce more-symmetric solutions and solution errors (where symmetry should be maintained) compared with the first-order reconstruction-based scheme. Importantly, the solution errors for the higher-order reconstruction schemes do not show significant dependence on the timestep, whereas the solution errors for the scheme using the first-order reconstruction show a strong dependence. The solution accuracy for the schemes using the higher-order reconstructions is better than that produced with schemes using a more-accurate estimate of the mass-flux region such as LR05 and Yeh (2007). This indicates that the errors in the schemes using first-order scalar reconstructions are dominated by errors in this reconstruction and not geometrical errors in determining the fluxed mass area.

We have confirmed the results presented in the thesis of L02. Specifically, we have verified the importance of the constraints that the least-squares-fit polynomial pass through the central cell value, and that the integral of the polynomial over the cell must equal the cell-averaged value times the area of the cell. We satisfy these constraints in a two step procedure, first fitting the polynomial subject to the first constraint and then adjusting the constant to satisfy the second, whereas L02 builds these into his weighted least-squares minimization procedure. The results presented herein and in L02 are very similar, hence both approaches are viable.

We have subjected the reconstruction-based schemes to a more-demanding deformational flow test based on the 2D planar deformational flow test used by Blossey and Durran (2008).

The tests show that these schemes using the polynomial reconstructions are robust. As expected, all the schemes possess convergence rates of approximately 2 or less as indicated in the deformational flow tests, whereas the cosine-bell solid body rotation tests of M07 and those for schemes using higher-order reconstructions reported here show convergence rates approaching 3 for the time-independent non-deformational velocity field.

Finally, we have qualitatively examined scheme efficiency, and we find that the scheme using the second-order reconstruction is significantly more efficient than either the schemes using the first or fourth-order reconstructions. The fourth-order reconstruction based scheme is very expensive because of the larger stencil used in the reconstruction, the need for higher-order polynomial evaluation, and the need for fourth-order accurate quadrature. Based on these results, we recommend using the second-order reconstruction in this scheme.

Acknowledgments.

We would like to thank Dr. Hilary Weller for bringing the Lashley (2002) dissertation to our attention, and for her careful review of this paper. We would also like to thank Dr. Hiroaki Miura for his careful review of this paper. Author Skamarock would like to acknowledge the Max Planck Institute for Meteorology in Hamburg, Germany and Dr. Almut Gassmann for supporting a short visit during which some of this work was accomplished. Author Menchaca performed this work under the auspices of the Significant Opportunities in Atmospheric Research and Science (SOARS) Program at the University Corporation for Atmospheric Research (UCAR) during the summer of 2009.

REFERENCES

- Blossey, P. N. and D. R. Durran, 2008: Selective monotonicity preservation in scalar advection. *J. Comp. Phys.*, **227**, 5160–5183.
- Lashley, R. K., 2002: Automatic generation of accurate advection schemes on unstructured grids and their application to meteorological problems. Ph.D. thesis, University of Reading, Reading, UK, 223 pp., [available at <http://www.reading.ac.uk/math/research/math-phdtheses.aspx>].
- Lipscomb, W. H. and T. Ringler, 2005: An incremental remapping transport scheme on a spherical geodesic grid. *Mon. Wea. Rev.*, **133**, 2235–2250.
- Majewski, D., et al., 2002: The operational global icosahedral-hexagonal gridpoint model gme: Description and high-resolution tests. *Mon. Wea. Rev.*, **130**, 319–338.
- Miura, H., 2007: An upwind-biased conservative advection scheme for spherical hexagonal-pentagonal grids. *Mon. Wea. Rev.*, **135**, 4038–4044.
- Skamarock, W. C., 2006: Positive-definite and monotonic limiters for unrestricted-time-step transport schemes. *Mon. Wea. Rev.*, **134**, 2241–2250.
- Strang, G., 1980: *Linear Algebra and Its Applications*. 2d ed., Academic Press, 414 pp.
- Stroud, A. H., 1971: *Approximate Calculation of Multiple Integrals*. Prentice-Hall, 431 pp.

- Stuhne, G. R. and W. R. Peltier, 1996: Vortex erosion and amalgamation in a new model of large scale flow on the sphere. *J. Comp. Phys.*, **128**, 58–81.
- Tomita, H., M. Tsugawa, M. Satoh, and K. Goto, 2001: Shallow water model on a modified icosahedral geodesic grid by using spring dynamics. *J. Comp. Phys.*, **174**, 579–613.
- Tremback, C. J., J. Powell, W. R. Cotton, and R. A. Pielke, 1987: The forward-in-time upstream advection scheme - extension to higher orders. *Mon. Wea. Rev.*, **115**, 540–555.
- van Leer, B., 1977: Towards the ultimate conservative difference scheme. iv. a new approach to numerical conservation. *J. Comp. Phys.*, **23**, 276–299.
- Williamson, D. L., 2007: The evolution of dynamical cores for global atmospheric models. *J. Meteorol. Soc. Jpn.*, **85B**, 241–269.
- Williamson, D. L., J. Drake, J. J. Hack, R. Jakob, and P. N. Swarztrauber, 1992: A standard test set for numerical approximations to the shallow-water equations in spherical geometry. *J. Comp. Phys.*, **102**, 211–224.
- Woodward, P. R. and P. Colella, 1984: The numerical simulation of two-dimensional fluid flow with strong shocks. *J. Comp. Phys.*, **54**, 113–173.
- Yeh, K.-Y., 2007: The streamline subgrid integration method: I. quasi-monotonic second-order transport schemes. *J. Comp. Phys.*, **225**, 1632–1652.
- Zalesak, S. T., 1979: Fully multidimensional flux-corrected transport algorithms for fluids. *J. Comp. Phys.*, **31**, 335–362.

List of Tables

- 1 Gauss quadrature points and weights for integrating a function over the interval $-1 \leq x \leq 1$. 24
- 2 Mesh and parameters for the cosine bell and deformational flow test case simulations. 25

TABLE 1. Gauss quadrature points and weights for integrating a function over the interval $-1 \leq x \leq 1$.

order	x_i	w_i
1	0	2
2	$\pm\sqrt{1/3}$	1
4	$\pm \left(\sqrt{3 - 2\sqrt{6/5}} \right) / 7$	$(18 + \sqrt{30}) / 36$
	$\pm \left(\sqrt{3 + 2\sqrt{6/5}} \right) / 7$	$(18 - \sqrt{30}) / 36$

TABLE 2. Mesh and parameters for the cosine bell and deformational flow test case simulations.

cells	$\Delta x_{avg}(m)$	cosine bell $\Delta t(s)$	deformational flow $\Delta t(s)$
2562	480514	7200	
10262	240305	3600	900
40962	120158	1800	450
163842	60079	900	225
655362	30040		100

List of Figures

- 1 Schematic showing the 2D scalar mass flux regions for the Miura (2007) scheme (left) and the Lipscomb and Ringler (2005) scheme (right). The shaded areas show the mass fluxed through the cell edge e_{12} over a time step Δt . 28
- 2 Schematic showing a grid centered about cell 0. The dark-shaded cells (1-6) are used in the reconstruction of polynomials less than or equal to order 2. The lighter-shaded cells (7-17) are used in the reconstruction of polynomials order 3 and 4. 29
- 3 L_2 and L_∞ error norms for first, second and fourth order reconstructions after a single revolution of the cosine bell. The simulation parameters are listed in table 1. 30
- 4 Scalar field and error after one revolution of the cosine bell using first and second order reconstructions. The grid contains 10242 cells and has a mean cell spacing of approximately 240 km, and the latitude and longitude lines are drawn every 15° . 31
- 5 L_2 and L_∞ error norms for first and second order reconstructions after a single revolution of the cosine bell using a constant timestep of 50 s. 32
- 6 L_2 and L_∞ error norms for first and second order reconstructions after a single revolution of the cosine bell using a variable timestep on the 40962-cell mesh. 33
- 7 Scalar field initial condition and solutions after one revolution of the slotted cylinder using first and second order reconstructions. 34
- 8 Blossey and Durran (2008) test problem mapped to the sphere. 35

9	L_2 and L_∞ error norms for the spherical version of the Blossey and Durran test case using first, second and fourth order reconstructions. The simulation parameters are listed in table 2.	36
10	Solutions at time T for the Blossey and Durran (2008) test problem using first, second and fourth order reconstructions on 40962 and 163842-cell meshes. The thick black contours are the exact solution for $\psi = 100$ and 800.	37
11	L_2 error norms plotted as a function of normalized CPU time for the spherical version of the Blossey and Durran test case using first, second and fourth order reconstructions.	38

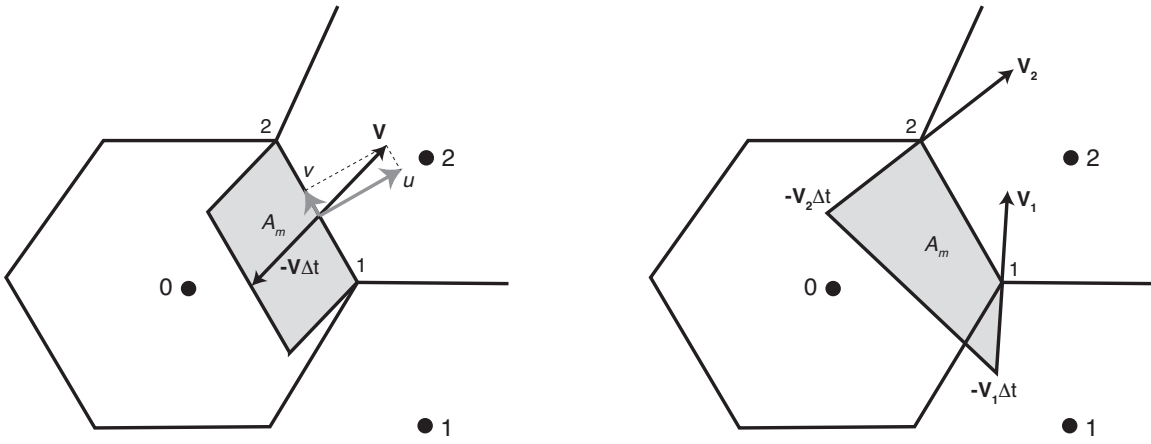


FIG. 1. Schematic showing the 2D scalar mass flux regions for the Miura (2007) scheme (left) and the Lipscomb and Ringler (2005) scheme (right). The shaded areas show the mass flux through the cell edge e_{12} over a time step Δt .

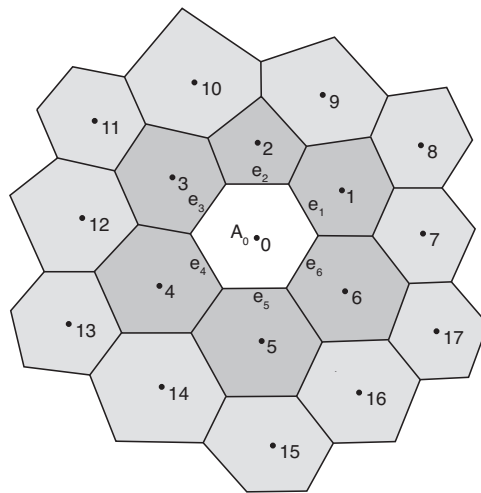


FIG. 2. Schematic showing a grid centered about cell 0. The dark-shaded cells (1-6) are used in the reconstruction of polynomials less than or equal to order 2. The lighter-shaded cells (7-17) are used in the reconstruction of polynomials order 3 and 4.

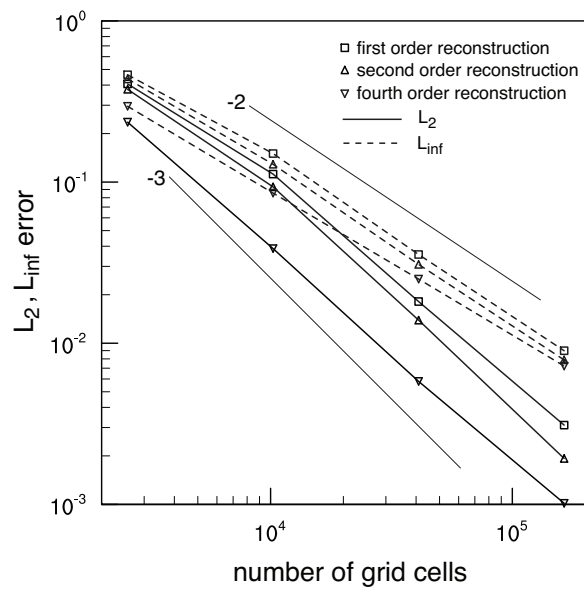


FIG. 3. L_2 and L_{∞} error norms for first, second and fourth order reconstructions after a single revolution of the cosine bell. The simulation parameters are listed in table 1.

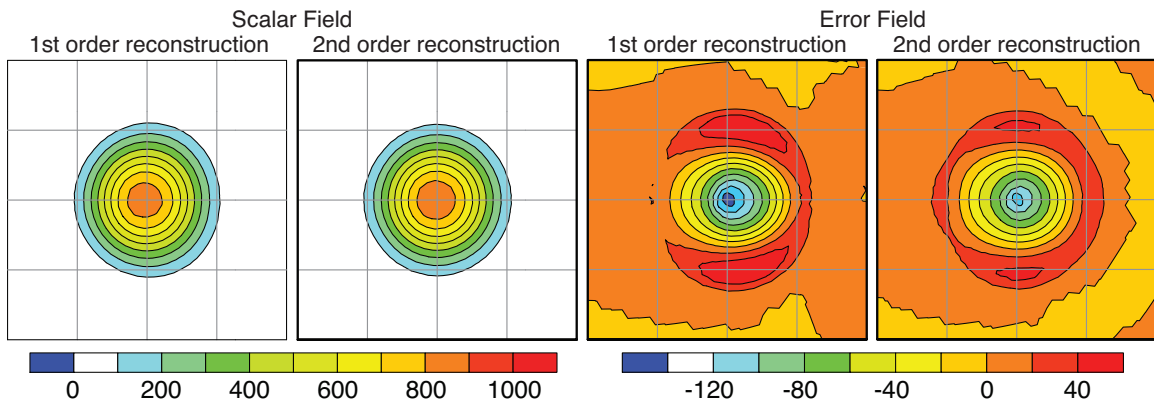


FIG. 4. Scalar field and error after one revolution of the cosine bell using first and second order reconstructions. The grid contains 10242 cells and has a mean cell spacing of approximately 240 km, and the latitude and longitude lines are drawn every 15° .

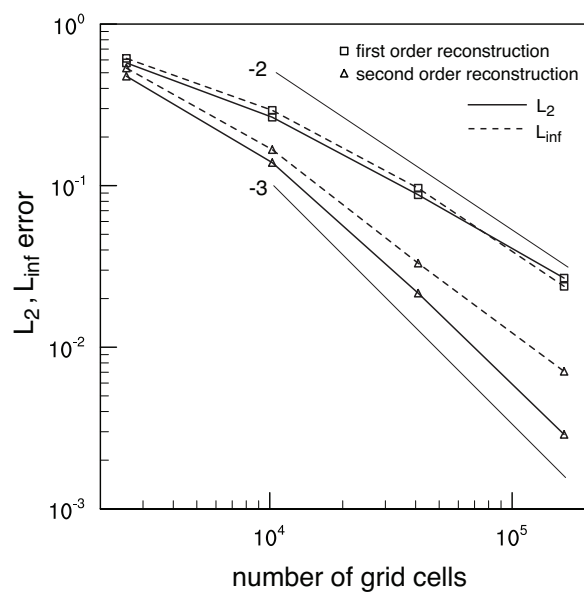


FIG. 5. L_2 and L_{∞} error norms for first and second order reconstructions after a single revolution of the cosine bell using a constant timestep of 50 s.

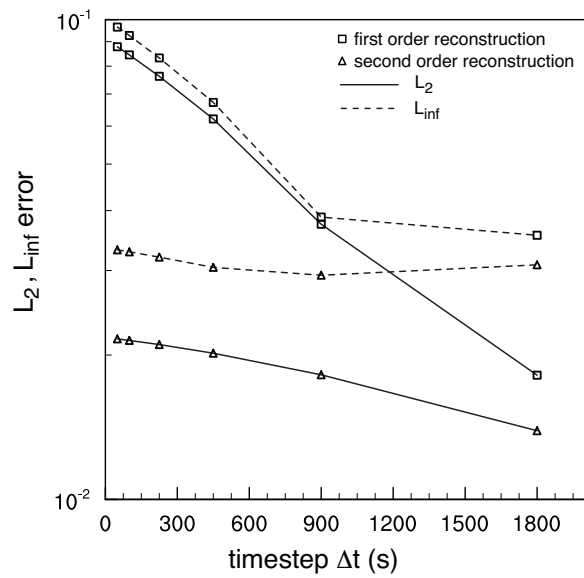


FIG. 6. L_2 and L_{∞} error norms for first and second order reconstructions after a single revolution of the cosine bell using a variable timestep on the 40962-cell mesh.

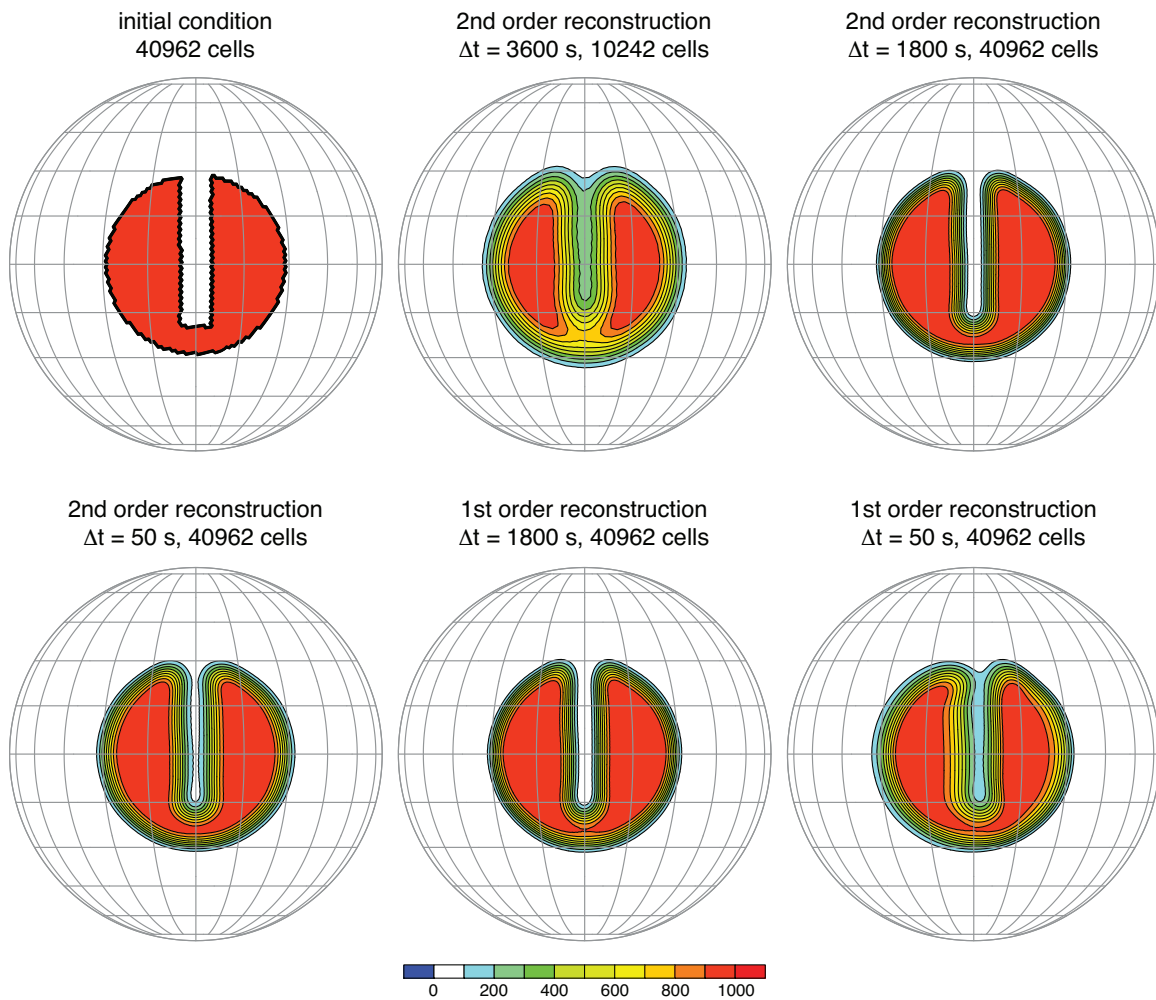


FIG. 7. Scalar field initial condition and solutions after one revolution of the slotted cylinder using first and second order reconstructions.

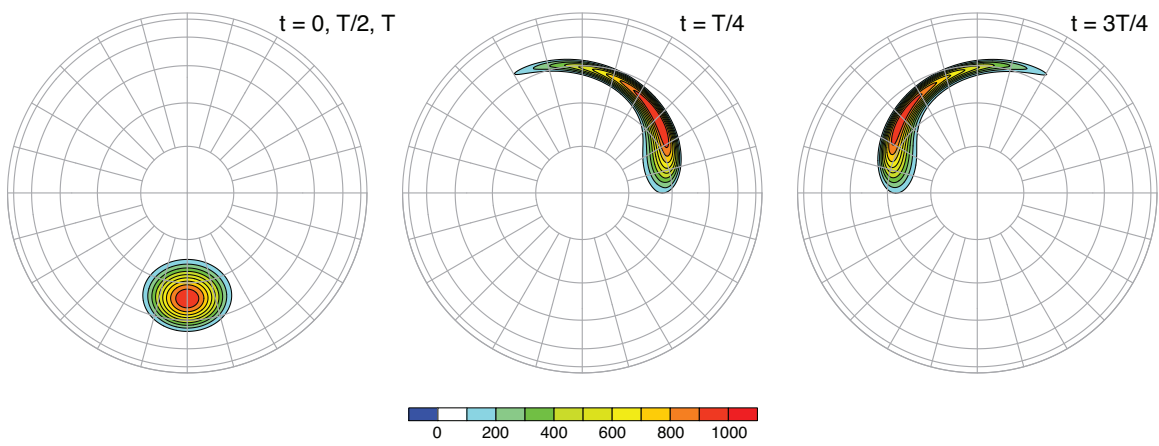


FIG. 8. Blossey and Durran (2008) test problem mapped to the sphere.

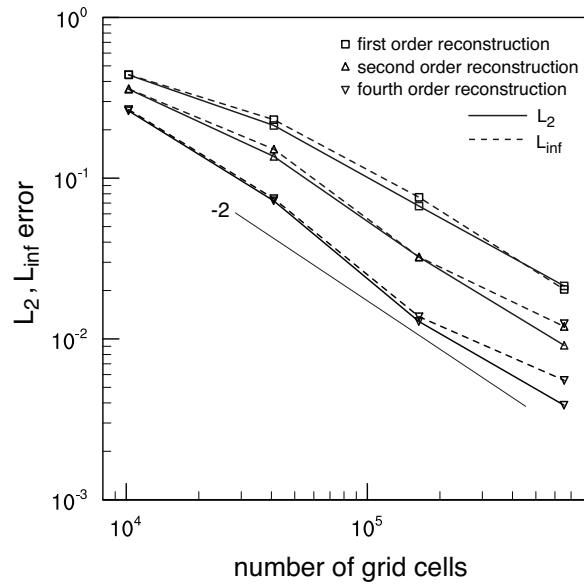


FIG. 9. L_2 and L_{∞} error norms for the spherical version of the Blossey and Durran test case using first, second and fourth order reconstructions. The simulation parameters are listed in table 2.

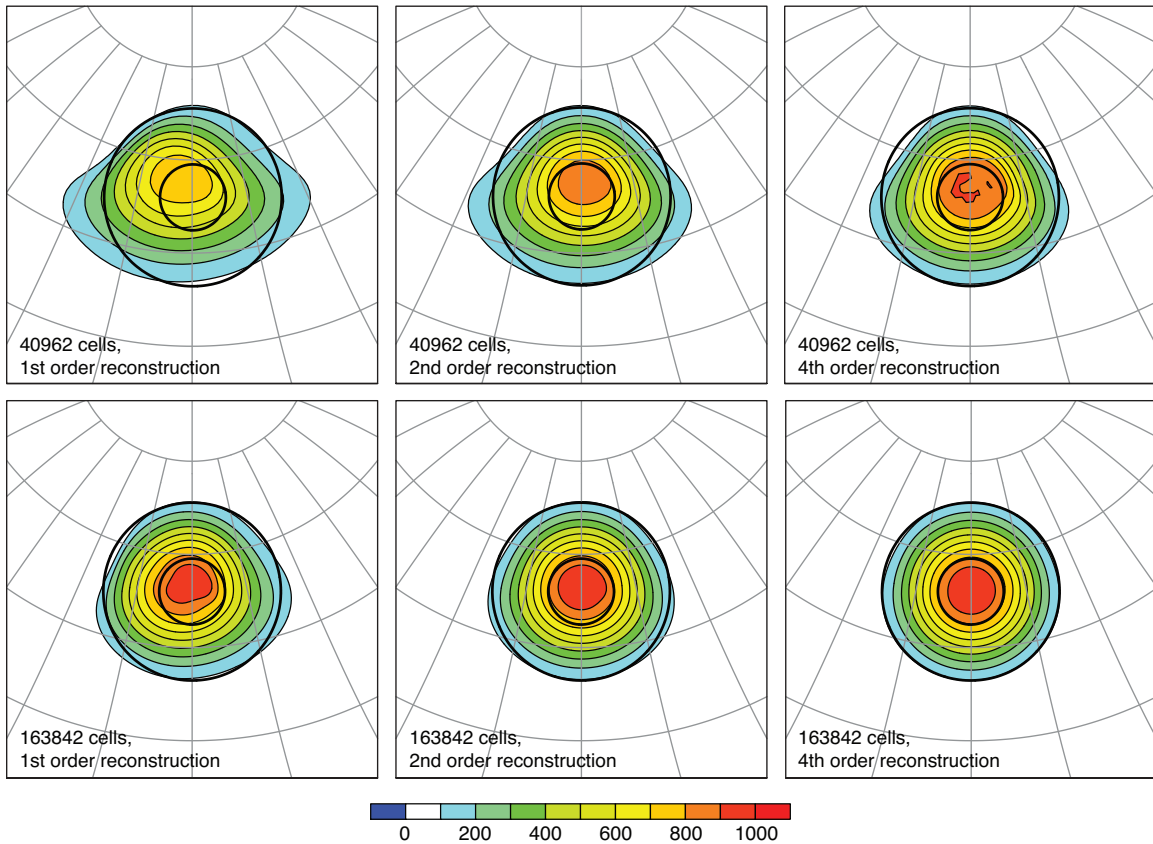


FIG. 10. Solutions at time T for the Blossey and Durran (2008) test problem using first, second and fourth order reconstructions on 40962 and 163842-cell meshes. The thick black contours are the exact solution for $\psi = 100$ and 800.

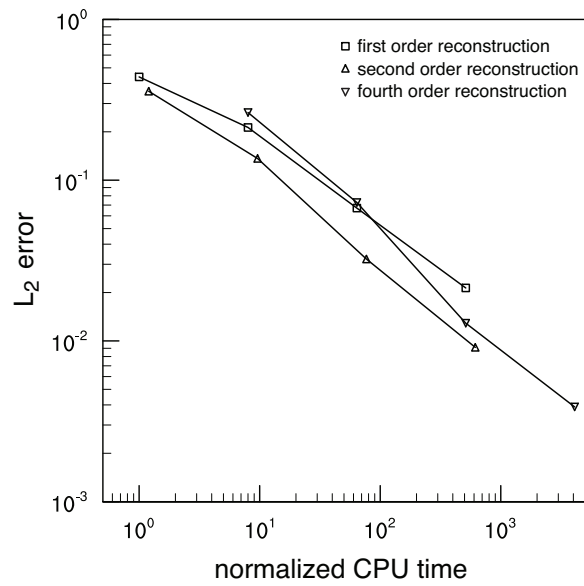


FIG. 11. L_2 error norms plotted as a function of normalized CPU time for the spherical version of the Blossey and Durran test case using first, second and fourth order reconstructions.